

2-hydroxy-4-amino-azobenzene modified Graphene Oxide with Incorporation of Bilirubin Oxidase for Photoelectrochemical Catalysis of Oxygen Reduction Reaction

Xueqing Chu, Mi Zhang, Wenshan Huo, Han Zeng, Yang Yang*

Xinjiang key laboratory of energy storage and photoelectrocatalytic materials, Chemistry and Chemical Engineering Academy, XinJiang Normal University, Urumuqi 830054, XinJiang Uyghur autonomous region, People's Republic of China

*E-mail: zenghan1289@163.com

Received: 25 July 2020 / Accepted: 8 September 2020 / Published: 30 September 2020

Bilirubin oxidase (BOD) molecules were firmly tethered on the surface of graphene oxide (GO) functionalized with 2-hydroxy-4-amino-azobenzene (AZO-1). Further, a BOD-based electrode was prepared through the immobilization of enzyme on the nanocomplex via drop casting. The morphology, structural properties, surface chemistry, and physiochemical features of the prepared nanocomplex were investigated by microscopic, spectrometric, electrochemical, and other characterization techniques. The as-prepared nanocomplex with enzyme incorporation exhibited high loading amount of redox protein molecule, excellent mechanical robustness, and thermal stability. The complicated mutual interaction between the nanocomplex and protein molecules led to a partial ordered conglomeration of enzyme molecules with micelle-like surface characteristics. The combination of cofactors within BOD and AZO-1 formed a composite with significantly suppressed fluorescence emission and inferior capability of electron transportation. Direct charge transfer in BOD-based electrode could be achieved with redox group of GO as the primary electroactive site. A considerable negative impact on the efficiency of electron transport, turnover frequency of substrate conversion, and incident light utilization for this redox-protein-based electrode was verified. However, the as-prepared BOD-based electrode exhibited high affinity to oxygen molecules, and the oxygen binding was not hampered severely in the presence of ligation between adjacent heteroatoms within AZO-1 and T₁ site in BOD.

Keywords: 2-hydroxy-4-amino-azobenzene, graphene oxide, bilirubin oxidase, photoelectrochemical catalysis, oxygen reduction reaction

1. INTRODUCTION

The effective utilization of solar energy has attracted global interest for addressing the electricity deficiency in underdeveloped and remote regions that lack power grids. The key factors that

govern the photoelectrocatalytic performance are the conversion efficiency of incident irradiation into electrons and the electron transfer efficiency [1-3]. Enzymatic electrochemical devices exhibit several advantages as high selectivity to specific substrate, excellent catalytic performance, and minimal environment influence. However, most enzyme-based electrochemical devices cannot utilize solar energy efficiently, and common artificial photocatalytic materials cannot show selectivity for a specific reaction. Therefore, a combination of biocatalysts such as enzymes and DNA and artificial photocatalytic materials can serve as a promising approach to develop novel high-performance photocatalysts for bio-medical applications. Graphene oxide (GO) is a well-known carbon-based material, which is a typical planar nanosheet composed of sp^2 hybridized carbon atoms that are densely packed in a hexagonal honeycomb crystal lattice, [4-8]. Presently, GO is established as the thinnest nanomaterial. The unique structure of GO facilitates superior properties such as favorable dynamics of charge convection, large specific surface area, large thermal conductivity, high Young's modulus, and excellent biocompatibility, which improve the efficiencies of charge transport and electron-hole separation. Owing to these merits, GO is widely used as modification stock for manufacturing electrochemical devices [9-11]. Azobenzene and its derivatives are commonly used organic dyes that exhibit desirable reversibility of redox reaction and good photosensitivity. Isomers of this family of compound: azobenzene and quinone hydrazine, can play various roles in the process of photocatalysis and electron transfer. They can be used as an electron mediator (e.g., azino-benzothiazoline sulphonic acid diammonium salt) in enzyme-induced electrocatalysis [12-13]. GO containing azobenzene-like groups can improve the chemical stability of organic dye molecules [13]. Photosensitive nanocomposite with entrapped redox enzyme can be prepared by simultaneous coupling of azobenzene-like chemicals and redox protein molecules with GO, which can be realized only by proper modification of the surface groups of GO or the structure of azobenzene chemicals.

Bilirubin oxidase (BOD) belongs to the family of blue multi-copper oxidase (MCO). It exhibits several advantages such as excellent catalytic performance at physiological pH conditions, favorable selectivity to specific substrate, and outstanding endurance to halogens. It is a promising biocatalyst, which is suitable for bio-electrochemical reduction of oxygen under moderate pH values. Recent reports have indicated that the physiochemical features of MCO molecules incorporated into enzyme carrier whose surface is tailored by aromatic groups may be different from those of the native enzyme [14-18]. Several studies have focused on this issue, and few of them have attempted to characterize the interactions between enzyme and accommodation matrix [14,19-21]. A direct connection between MCO molecules and GO or the incorporation of MCO molecules in GO membrane can lead to a direct electron transport between cofactors (for e.g., T_1 Cu) and conductive matrix. The mechanisms of electron transport and enzyme-induced catalysis in GO with enzyme integration are similar to those for multi-wall carbon nano-tubes (MWCNTs) with protein entrapment [22]. The catalytic activity of GO with MCO immobilization is attenuated with time due to the distortion in the configuration of cofactors in MCO molecules. This is attributed to the complicated interactions between redox sites within MCO and enzyme carrier, which have a considerable impact on the nature of protein molecules. The alignment of enzyme molecules on the surface of protein carrier resulting from the mutual interactions between MCO and heteroatoms within azobenzene-like compound including adjacent ligation can facilitate electron transfer between redox sites within MCO and conductive matrix.

Furthermore, such interaction is helpful for the effective utilization of incident illumination. However, the influence of interactions between organic dyes as photosensitive element and protein molecules and the mechanism of photoelectrochemical catalysis needs to be further investigated [23-24].

In this study, surface-tailored GO using azobenzene derivatives is proposed as the enzyme matrix. BOD molecules are firmly tethered on GO by azobenzene groups to form nanocomposite with protein incorporation. Further, a BOD-based electrode is prepared using the nanocomplex on which enzyme is anchored via conventional drip-coating method. The conglomeration form of attached protein molecules, structural parameters, surface chemistry, and physiochemical features of nanocomplex with BOD integration and the configuration of cofactors within BOD are systematically investigated by multiple characterization techniques. Direct electrochemistry, sensitivity to dissolved O₂, and photo-electrocatalysis of oxygen reduction reaction (ORR) are also examined. Overall, this study provides useful insights into the mechanism of internal/external electron transmission within MCO as well as the principle of enzyme-induced catalytic reaction. Further, it can serve as practical reference for the development of novel photo-modulated electrochemical devices using carbon-based nanomaterials functionalized with small organic dye molecules.

2. EXPERIMENT

2.1 Reagents and characterization instruments

BOD from *M. Verrucaria* (molecular weight ~ 79000 g/mol; crystallization and purification were performed as described in an earlier study [22]), 2, 2'-azino-bis-(3-ethylbenzothiazoline-6-sulphonic acid) diammonium salt (ABTS), and 2, 6-dimethoxyphenol (DMP) were bought from Sigma Chemical Reagent Co., Ltd., USA. Chemicals and other routine reagents used in the synthesis and characterization of precursors and intermediates (e.g., Chitosan (CTS), deacetylation degree > 90%, molecular weight ~ 250000) were obtained from Sinopharm Co., Ltd., China. These chemical reagents were of analytic purity and were used as it is without further purification. Indium tin oxide (ITO) electrode was acquired from Kaiwei Photo-Electronic Tech. Ltd., Zhuhai, China. The ITO electrode was pretreated and then coated with poly-dimethylsiloxane membrane (PDMS) according to the procedure described in an earlier study [25]. GO was purchased from Aldrich, USA, and it played the roles of enzyme carrier and conductive support.

LG16-W high-speed centrifuge was provided by Beijing Jingli Centrifuge Co., Ltd., China. Hitachi z2000 type atomic absorption spectrometer is secured from HITACHI Company, Japan (main frame: single beam flame, equipped with graphite furnace atomic absorption spectrophotometer, range of absorption spectrum: 190~900 nm). H-800 type transmission electron microscope with accelerating voltage: 200.0 kV and SU8000 type scanning electron microscope under accelerating voltage: 5.0 kV are bought from HITACHI Company. The Fourier-transform infrared (FTIR) and ultraviolet-visible (UV-vis) spectra were obtained using a FTIR spectrometer (SENSOR-27, Bruker, Germany; KBr slice) and UV-vis spectrometer (U-3310, Shimadzu Corporation, Japan; optical length: 1 cm), respectively. STA409 PC type synchronized thermogravimetric analyzer is bought from Netzsch

Company, Germany. Spectropolarimeter equipped with a 150-W Xe lamp and air-cooling device is secured from Chirascan, Applied Photophysics, UK. Cary Eclipse spectrofluorometer (excitation wavelength: 280 nm, emission wavelength: 525 nm, slit width: 5 nm, wavelength scan range: 200-600 nm) was provided by Varian, USA. X'Pert PRO X-ray diffractometer is obtained from Philips, Holland. N₂ and O₂ with high purity (Nan-Jing Special Gas Industrial Co., Ltd, China) were used in all the electrochemical experiments. A glassy carbon basal electrode (GCE, diameter: 3 mm), reference electrode-Ag/AgCl in saturated KCl aqueous solution, and auxiliary one-platinum wire were acquired from Aida Hengsheng Industrial And Commercial Co., Ltd., China. The pretreatment process of GCE is described in earlier studies [26-27].

0.2 M phosphate buffer solution (PBS) was prepared and used as the buffer solution throughout the test. Its pH value was regulated according to a previous study [26]. All the potentials were measured with respect to normal hydrogen electrode (NHE) as standard point. Zahner Zennium and CHI-1140A electrochemical workstations were purchased from Kronach, Germany and CHI Inc., Chen-Hua Co., Ltd., Shang-Hai, China, respectively. AFMSRCE rotating disk electrode system was obtained from Pine, USA. The rotation speed of electrode ranged from 50 to 10,000 rpm.

2.2 Preparation and characterization of nanocomposite incorporated with BOD and BOD-based electrode

The azobenzene derivative, i.e., 2-hydroxy-4-amino-azobenzene (AZO-1) and GO functionalized by AZO-1 (denoted by GO-AZO-1) were prepared, purified, and characterized according to a previous study [28]. The as-prepared 2 mg powder of GO-AZO-1 was ultrasonically dispersed into a solution of dimethyl sulfoxide (DMF), and then 1.0 mg BOD was added into the uniformly distributed discrete phase under magnetic stirring for 30 min. The mixture was incubated in refrigerator overnight to allow adequate interaction between GO-AZO-1 composite and BOD molecules. Finally, the supernatant was centrifugally separated from the slurry at a centrifugation rate of 10000 rpm. The sediment was rinsed twice by PBS to remove any protein molecules unsteadily attached on the surface of protein matrix. The obtained precipitate was nanocomposite with BOD immobilization, which was denoted as BOD/GO-AZO-1. The as-prepared 20.0 μ L of BOD/GO-AZO-1 was pipetted onto the interface of supporting electrode. Consequently, the electrode was coated by a thin film of BOD/GO-AZO-1, which was then dried in a buckle beaker to prepare BOD-based electrode (i.e. BOD/GO-AZO-1/GC). The reference GO-AZO-1/GC electrode was prepared using a similar procedure except for the incorporation of enzyme into matrix. A hole with a diameter of 7 mm was made on PDMS thin film by a drill. The PDMS membrane with hole was mounted on the surface of ITO electrode. Subsequently, 40 μ L of BOD/GO-AZO-1 fluid was dropped into the hole, and it was dried in air. Finally, 10 μ L CTS was pipetted onto the thin film of BOD/GO-AZO-1 and ITO electrode capped by nanocomplex with BOD attachment was dried in a beaker under atmospheric pressure and room temperature to obtain BOD/GO-AZO-1/ITO. The preparation of photocatalyzed ITO electrode based on BOD/GO-AZO-1 is illustrated in Fig.1.

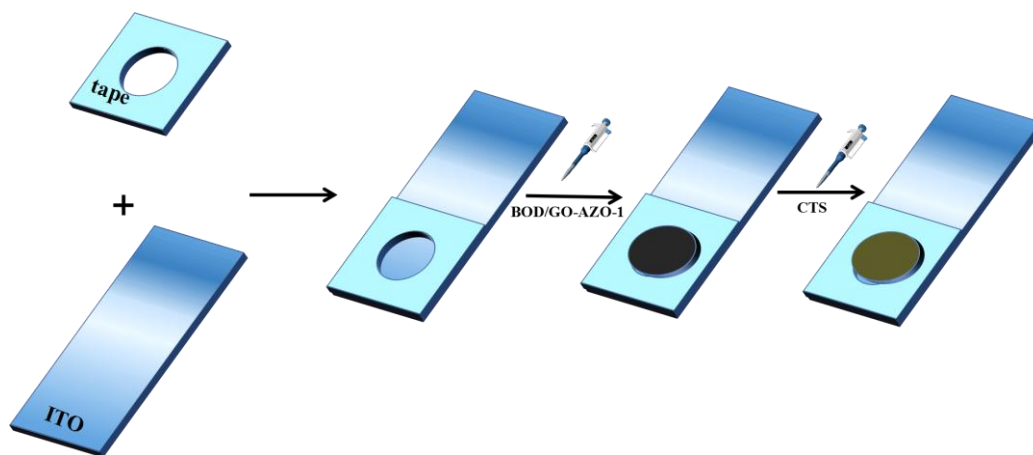


Figure 1. Schematic for the preparation of ITO electrode based on GO-AZO-1 nanocomplex with BOD incorporation (BOD/GO-AZO-1)

The enzyme loading of matrix was obtained with GFAAS [29] using the variation of copper content in the bulk solution containing enzyme molecules before and after the integration of enzyme into GO-AZO-1. It should be noted that molar ratio of copper vs. BOD molecule was 4:1. The morphological features, surface chemistry, and interactions between nanocomplex and entrapped BOD were characterized using SEM, TEM, and FTIR spectroscopy. For TEM test, the samples were prepared as follows: dispersed phases of samples (i.e., GO, GO-AZO-1, and BOD/GO-AZO-1, PBS with pH = 4.4 as dispersant) were dripped onto the copper mesh and they were then dried under vacuum. For SEM test, traces of dry powders (GO, GO-AZO-1, and BOD/GO-AZO-1) were fixed on a platinum sample seat with conductive adhesive to prepare the testing samples. The variation in the configuration of cofactors within BOD before and after the integration of enzyme molecules into protein carrier was explored by UV-vis spectrophotometry [30]. The interaction between nanocomplex and BOD was investigated by fluorescence spectrometry (FRS). FRS measurement was conducted as follows: variable amounts of AZO-1 and constant amount of enzyme were dissolved into a solvent via magnetic stirring. The eutectic mixtures were pre-scanned to ensure appropriate excitation and emission wavelengths. The variation in the crystal phase of GO-AZO-1 nanocomplex before and after the integration of BOD was probed by XRD. XRD measurements were conducted under the following conditions: voltage = 30 kV, current = 10 mA, nickel filtered K- α radiation from copper target (wavelength $\lambda = 0.154$ nm), and sweep rate = $4^\circ/\text{min}$. The mechanical strength, thermal stability, and hydrophilicity of BOD/GO-AZO-1 were investigated by UV-vis spectroscopy, GFAAS, TGA, and circular dichroism (CD), respectively. The robustness of BOD/GO-AZO-1 was measured using a method described earlier [26]. Briefly, this method can be explained as follows: BOD/GO-AZO-1 was magnetically stirred in PBS with pH = 6.0 for 5 min. The enzyme supporter was centrifugally separated from the system at a rotation speed of 8000 rpm. Subsequently, 100.0 μL of 10.0 mM DMP solution was injected into the supernatant. Eventually, the variation in absorbance of solution at 470.0 nm with time was recorded. Similarly, the content of copper within the supernatant after centrifugation isolation of enzyme matrix from the discrete product was measured to assess the robustness of

BOD/GO-AZO-1. TGA was performed under the following conditions: nitrogen atmosphere, variation rate of temperature = 10.0 °C/min, range of temperature variation = 298-1173 K. PBS with dissolved BOD, evenly dispersed GO-AZO-1 in PBS, and BOD/GO-AZO-1 were selected as CD testing samples under moderate sweep range of wavelength.

2.3 Direct electrochemistry, enzyme-induced electrochemical reduction of oxygen molecule, and photoelectrochemical catalysis for BOD-based electrode

The active surface areas of the as-prepared electrodes were determined as 0.20 and 0.18 cm² using an earlier presented method [31]. The variation in the electrical conductivity of nanocomplex-based electrode before and after BOD immobilization was monitored by electrochemical impedance spectrometry (EIS) and cyclic voltammetry (CV). The EIS measurements were conducted under the following parameters: open circuit voltage = 436 mV, frequency range = 0.1-10⁵ Hz, amplitude of excitation signal = 5.0 mV. All electrochemical experiments were performed in a standard electrolytic cell consisting of three electrodes. BOD-based electrode (i.e., BOD/GO-AZO-1/GC) acted as a working electrode. CV and differential pulse voltammetry (DPV) were used to explore direct electrochemistry of BOD/GO-AZO-1/GC in oxygen-free electrolyte. DPV curves were obtained under the following parameters: measurement range of potential = -1.0-1.0 V, step potential = 5 mV, and pulse interval = 0.05 s. Catalytic efficiency of BOD-based electrode toward ORR was evaluated by CV and chronoamperometry (CA). The CA curve of BOD-based electrode in electrolyte containing variable consistencies of oxygen molecules under constant applied potential was obtained by measuring the current response as a function of time. PBS with variable consistencies of oxygen molecule was prepared using an earlier described method [32]. The content of dissolved oxygen molecules was determined by Clark oxygen electrode (Hansatech, UK). The applied potential for CA experiment was chosen according to an earlier study [33]. All electrochemical experiments were conducted at atmospheric pressure (94.8 kPa) and room temperature (22.5±0.6 °C). A 300-W Xe lamp equipped with UV cutoff filter (420 nm) was used as the visible light source. The distance between the irradiation source and reaction tube was adjusted to 80 mm for accommodating substrate and photocatalytic element (i.e., BOD/GO-AZO-1). Before light illumination, the BOD/GO-AZO-1 matrix was immersed in PBS saturated with oxygen, which was magnetically stirred in a darkroom for 1 h to ensure equilibrium of adsorption and desorption. Subsequently, the system was exposed to the irradiation source for a certain period, and the current density response of photocatalysis with irradiation time was recorded. "On" and "Off" states were switched at different time intervals through turn-off and turn-on of light source. To evaluate the stability of the prepared photocatalyst, it was recycled in electrochemical reduction of enzyme-induced ORR. The matrix with photocatalyst was removed from the reaction system and stored in a refrigerator at 4 °C when it was not in use.

3. RESULTS AND DISCUSSION

3.1 Morphology, structural features, and physiochemical properties of BOD/GO-AZO-1

The amount of BOD in the nanocomplex was determined as 297.5 mg/L, which was much higher than that of BOD attached on GO (86.4 mg/L) and BOD tethered to AZO-1 (122.5 mg/L). Such high loading amount of BOD into the matrix should be attributed to the synergistic effect of mutual interactions between enzyme carrier and BOD (i.e., covalent bonding, adjacent complexation, and π - π stacking effect), which can lead to the formation of a partial orientated array of redox protein molecules on the protein immobilization matrix. This can be validated through the TEM and SEM images of GO (A and D), GO-AZO-1 (B and E), and BOD/GO-AZO-1 (C and F) in Fig.2. Fig.2A reveals flocculent blocks with obvious fringes and less layers in GO, which exhibits a silky and undulating structure. Furthermore, bright fringe and dark inner portion can be seen in Fig.2A and Fig.2D. The darkness of GO is intensified after functionalization with AZO-1, and the stratification of GO-AZO-1 is more prominent. The inner interface of flocculent structure in GO-AZO-1 is rather rough, and relatively small clots on a subregion in the inner part for GO with AZO-1 functionalization can be discerned in Fig.2B and Fig.2E. The apparent increase in the darkness of inner surface and small conglomeration of inner section for GO functionalized by AZO-1 can be attributed to the synergistic effect of covalent bonding between GO and AZO-1 and π - π stacking effect between AZO-1 and hydrophobic surface of GO or attached azobenzene molecules. The morphology of BOD/GO-AZO-1 is completely different than that of GO and GO-AZO-1. It is evident that the original flocculent unit of GO is replaced by large amorphous clusters to a great extent (see Fig.2C), and the number of layers in BOD/GO-AZO-1 is much higher than that in GO (see Fig.2F).

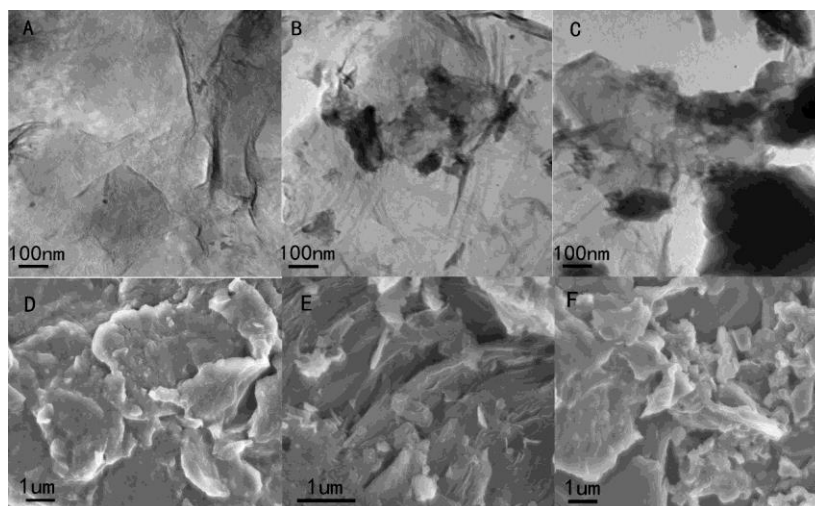


Figure 2. TEM (A-C) and SEM (D-F) images of GO (A and D), GO-AZO-1 (B and E), and BOD/GO-AZO-1 (C and F)

It should be noted that huge aggregations are composed of smaller quasi-spherical clusters. Such feature of BOD/GO-AZO-1 is rather similar to that of redox protein molecules attached on the

interface of GO [34]. It should be attributed to the partially ordered distribution of BOD molecules on the surface of enzyme carrier resulting from the cooperative effect of π - π stacking effect and abutting coordination between heteroatoms within AZO-1 and central Cu ion in BOD.

The FTIR spectra of GO, AZO-1, GO-AZO-1, BOD/GO-AZO-1, and free BOD are shown in Fig.3A. The observed peaks in the spectra of GO and AZO-1 are consistent with earlier reports [28, 35]. The peak at 1731.9 cm^{-1} in the spectrum of GO corresponds to the stretching vibration of -C=O in carboxylic group, an the characteristic peaks at 1384.8 , 3317.3 , and 3656.2 cm^{-1} in the spectrum of AZO-1 represent -N=N- , -NH , and -OH stretching vibrations, respectively. Moreover, the existence of -C=N stretching vibration at $\sim 1634\text{ cm}^{-1}$ proves that AZO-1 is a mixture of azobenzene and quinone hydrazone [36]. In the spectrum of GO-AZO-1 (curve c) in Fig.3A, the characteristic peaks at 1233 and 1569.9 cm^{-1} correspond to C-O-C and -C=O stretching vibrations in ester. Accordingly, it can be inferred that AZO-1 is covalently linked to GO via the formation of ester bond. Furthermore, the locations of characteristics peaks corresponding to -C=O in carboxylic group and -NH in the structural unit of AZO-1 remain intact after linkage of AZO-1 to GO. This suggests that the excess group in AZO-1 is retained to immobilize enzyme molecules through covalent bonding. However, the peak corresponding to -N=N- stretching vibration ($\sim 1360\text{ cm}^{-1}$) is shifted toward long wavelength due to the connection between AZO-1 and huge π electron conjugation system in GO. The spectrum of BOD/GO-AZO-1 is quite different than that of GO, AZO-1, GO-AZO-1, and free BOD. The strong peak at $\sim 3427\text{ cm}^{-1}$ corresponding to -NH stretching vibration in amido bond and the overlapping peaks at $\sim 1634\text{ cm}^{-1}$ corresponding to -C=O in amido bond and -C=N in quinone hydrazone indicate that BOD molecules is covalently tethered to the bonding groups (i.e. -COOH groups) on the surface of GO via the formation of amido bond.

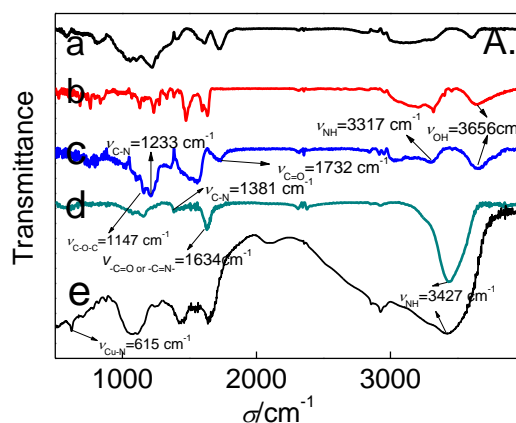


Figure 3. A FTIR spectra of GO (a), AZO-1 (b), GO-AZO-1 (c), BOD/GO-AZO-1 (d), and BOD (e)

This is supported by the presence of a peak representing amido bond in the spectrum of free BOD, as shown in the curve e of Fig.3A. The original peak at 615.0 cm^{-1} corresponding to Cu-N vibration in the spectrum of free BOD vanishes after the incorporation of BOD into GO-AZO-1 composite. This can be attributed to the interference of neighboring coordination between Cu ions of redox sites in BOD and N atoms in amido group of nanocomplex. It should be noted that a stronger peak representing -C=N as compared to that representing -N=N- and a stable peak at 1147.0 cm^{-1}

corresponding to $-C-N$ stretching vibration can be observed in curve d of Fig.3A. This indicates that the connection between GO-AZO-1 and BOD is helpful in maintaining the dominance of quinone hydrazone configuration in AZO-1 structure. The interaction between BOD and AZO-1 can have a significant impact on the optical response of BOD/GO-AZO-1. Such interactions can also influence the configuration of BOD similar to electron transport mechanism and catalytic kinetics [26].

The UV-vis spectra of GO, AZO-1, GO-AZO-1, BOD/GO-AZO-1, and free BOD are shown in Fig.3B (a-e), respectively. A broad peak at ~ 250 nm in the spectra of GO and AZO-1 can be ascribed to $\pi-\pi$ electron transition of carbon backbone $-C=C-$ or aromatic ring. Prominent peak at ~ 437.7 nm representing quinone hydrazone configuration of AZO-1 has a higher intensity than that representing azobenzene isomer, as shown in curve b of Fig.3B. Only one wide peak at ~ 255 nm corresponding to $\pi-\pi$ electron transition of aromatic ring in AZO-1/ sp^2 hybridized carbon atoms in GO can be identified in curve c of Fig.3B. A slight red shift of this characteristic peak can be due to the formation of gigantic π electron conjugation system via covalent bonding between AZO-1 and GO. Furthermore, the vanishing of band at ~ 437.7 nm representing quinone hydrazone can be attributed to internal electron transfer between chromophore group: AZO-1 and GO due to the formation of gigantic conjugation system via ester bond [35].

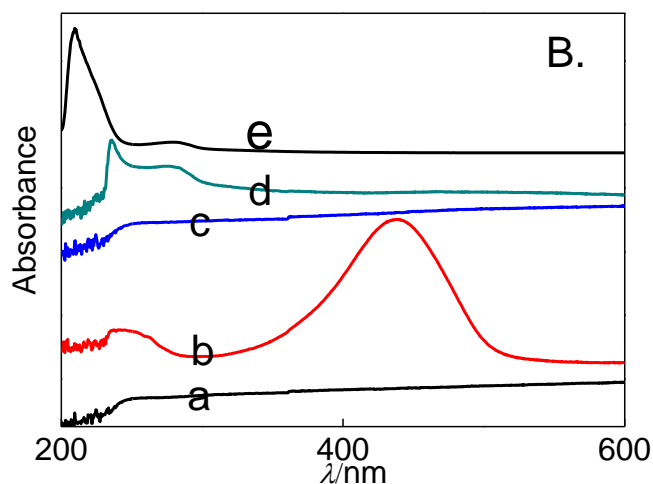


Figure 3. B UV-vis spectra of GO (a), AZO-1 (b), GO-AZO-1 (c), BOD/GO-AZO-1 (d), and free BOD (e)

The weak absorbance peak at 280.8 nm in curve d of Fig.3B corresponds to typical $n \rightarrow \pi^*$ electron transition in $C=O$, and the peak intensity of BOD/GO-AZO-1 is higher than that of free BOD (curve e in Fig.3B) due to the introduction of additional amido bonds between AZO-1 and GO. The band at 210.3 nm corresponding to $\pi \rightarrow \pi^*$ electron transition in T_1 site of free BOD disappears after the incorporation of BOD into GO-AZO-1 nanocomposite. Simultaneously, new absorbance peak at 235.9 nm is observed in curve d of Fig.3B. All these observations can be attributed to abutting ligation between Cu ion in T_1 site of BOD and heteroatoms in elements of nano-complex. Such interaction leads to a red shift in the peak representing $\pi \rightarrow \pi^*$ electron transition for aromatic ring of AZO-1 in conjugation with huge π electron system. It should be noted that the magnitude of this red shift in the presence of adjacent complexation is obviously lower as compared to that of BOD connected with GO

(i.e., similar red shift of peak representing $\pi \rightarrow \pi^*$ electron transition is ~ 50.8 nm, not shown in the figure). The proportion of enzyme leakage from protein carrier in the total enzyme loading for BOD accommodation matrix is minor (less than 1.5%). Result of UV-vis experiment implies that amplitude of increase in absorbance is less than 0.02 within 50 sec. All these results verify the excellent mechanical stability of BOD/GO-AZO-1.

Fig.3C shows the fluorescence emission spectra of solutions composed of a fixed amount (0.04 mg/mL) of BOD and variable concentrations of AZO-1. An apparent band at the excitation wavelength of 336.0 nm for the solution containing just BOD should be attributed to the presence of amino acids near T_1 Cu site of BOD (i.e. Tyr, Trp, and Phe) [37]. Intensity of this emission band decreases drastically with the increase in the consistency of AZO-1 in the mixture of BOD and AZO-1. It can be inferred from Fig.3C that binding of BOD with AZO-1 via adjacent coordination can form a composite that does not fluoresce. The rate constant of fluorescence quenching (K_q) is evaluated as 1.538×10^{11} L/(mol s) according to the Stern-Volmer equation [37]. The fluorescence quenching to BOD due to AZO-1 can be assigned to typical static quenching mode for the rate constant of fluorescence quenching much higher than the threshold value of K_q for usual quenching reagents of bio-macromolecules (2.0×10^{10} L/(mol s)).

Moreover, the binding site of BOD with AZO-1 is obtained as 1 by data processing [37]. This value is consistent with the structural characteristics of BOD molecule (only single Cu ion of T_1 site in BOD can interact with AZO-1 [38]). The apparent binding constant is calculated as 1.54×10^3 L/mol, which is much lower than that of protein combined with organic dye (3.84×10^7 L/mol) [37]. This implies that the interaction between cofactor in BOD and AZO-1 is not too strong to impose a serious impact on the intrinsic catalytic function of BOD for a short period.

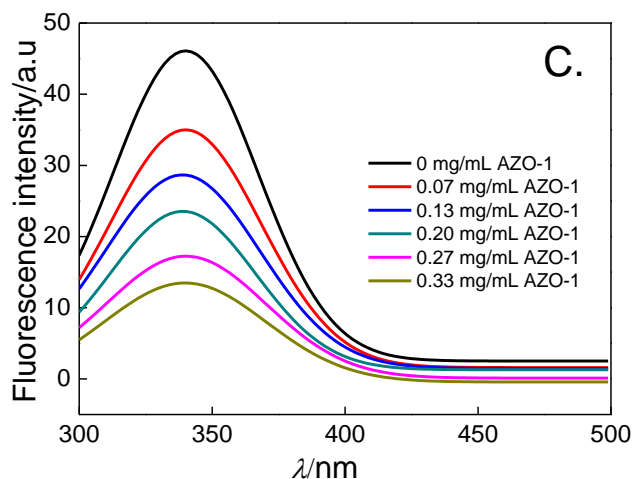


Figure 3. C Fluorescence spectra of solutions composed of 0.04 mg/mL BOD and variable concentrations of AZO-1

The XRD spectra of GO, GO-AZO-1, BOD powder, and BOD/GO-AZO-1 are illustrated in Fig.3D. The intrinsic peak of GO at $2\theta = 11.0^\circ$ corresponding to (0 0 1) plane disappears, and a new diffraction peak at 25.8° for (0 0 2) plane of graphite emerges after the incorporation of AZO-1 in GO

via chemical bonding. This can be ascribed to the reduction in redox current due to the addition of SOCl_2 [35]. Two characteristic peaks: one sharp peak at 17.9° and a weak one at 42.7° , can be observed in the spectra of GO-AZO-1 and AZO-1 powder (data not provided). This indicates that the original crystal structure of AZO-1 remains intact after the incorporation of AZO-1 in GO. Two broad and faint diffraction bands at $2\theta = 17.9^\circ$ and 29.2° corresponding to the abundant glycosylation groups and aromatic hetero-ring groups near T_1 site (e.g., His) in BOD (i.e., inferior degree of crystallinity) can be observed in the spectrum of free BOD. Most diffraction peaks in the spectrum of BOD/GO-AZO-1 are identical to those in the spectra of free BOD and GO-AZO-1. It may be noted that the intensity of diffraction peak at 28.9° is enhanced after the integration of BOD in the nano-complex. This can be attributed to covalent linkage and adjacent ligation as described previously. Such mutual interactions can improve the crystallinity and increase the orderliness of BOD/GO-AZO-1.

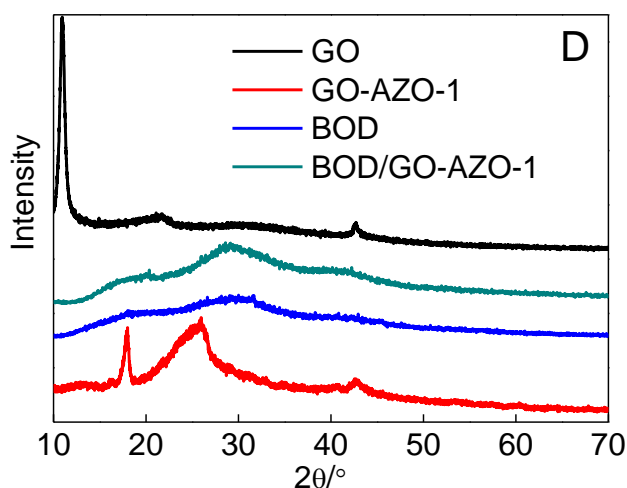


Figure 3. D XRD patterns of GO, BOD, GO-AZO-1, and BOD/GO-AZO-1

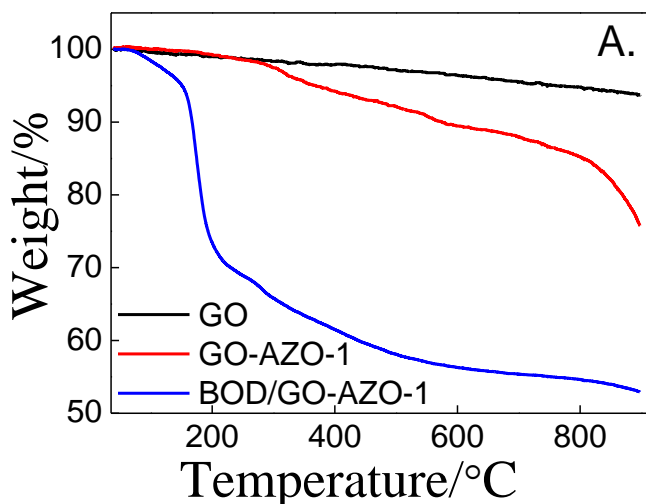


Figure 4. A TGA curves of GO, GO-AZO-1, and BOD/GO-AZO-1

Fig.4A depicts the TGA curves of GO, GO-AZO-1, and BOD/GO-AZO-1. An extremely low weight loss of GO is observed during the entire heating process. This can be attributed to the thermal decomposition of functional groups (i.e., decarboxylation) at the defect of graphene fringe under high temperature. Thermal decomposition of GO-AZO-1 can be divided into two stages, which include breakdown of $-N=N-$ and ester bond [28] initiating at 290.3 and 815.6 °C, respectively. TGA curve of BOD/GO-AZO-1 is quite different from that of GO and GO-AZO-1. First, thermal decomposition commences at a lower temperature of 72.8 °C, and subsequent thermal decomposition occurs at 155.4 °C. The total mass loss is ~30.0% at the end of second decomposition, which is consistent with the determined enzyme loading of matrix based on GFAAS. Both processes of thermal decomposition are related to the detachment of BOD from enzyme supporter. The first decomposition stage represents thermal desorption of weakly attached BOD molecules on the nanocomposite, and the second stage is attributed to the destruction of amido group between BOD and GO-AZO-1. Similar signatures of thermal disruption in $-N=N-$ and ester bond can be observed in the TGA curve of BOD/GO-AZO-1.

CD spectra of free BOD, GO-AZO-1, and BOD/GO-AZO-1 are shown in Fig.4B. Only one negative absorption band at 217.6 nm for hydrophobic α -helix can be observed in the spectrum of free BOD. Two prominent negative absorbance peaks at 207.2 and 210.0 nm can be observed in the CD spectrum of GO-AZO-1. These negative bands can be related to the hydrophobic units in AZO-1 and GO [38-39] as similar absorption peaks are observed in the spectra of GO and AZO-1 (data not shown). A relatively sharp negative band at 206.1 nm can be observed in the CD spectrum of BOD/GO-AZO-1. This band is slightly blue-shifted with respect to the one of GO-AZO-1, and the intrinsic band of free BOD at 217.6 nm suggests the presence of abutting complexation of T_1 Cu site in BOD with heteroatoms of GO-AZO-1. The disappearance of original absorbance band corresponding to free BOD also indicates the unique structural feature of BOD/GO-AZO-1, which is consistent with previous electron micrograph analysis. This suggests that orientated binding of T_1 site in BOD molecule with AZO-1 on the surface of GO can lead to the formation of micelle-like structural unit with hydrophilic outer surface and hydrophobic inner core. The hydrophilicity of BOD immobilized on the carrier is improved remarkably. The results of dispersion test also support this conclusion. Highly dispersed discrete nanoparticles of BOD/GO-AZO-1 in aqueous solution could be retained for 3 weeks. The dispersion of GO with BOD attachment could be maintained for only 4 days, and then it began to coagulate. Complete coagulation occurred after 8 days of incubation.

The EIS spectra of four secured electrodes in static PBS containing electro-chemical probing species and the corresponding CV curves in the same electrolyte recorded at a moderate scanning rate are shown in Fig.4C and Fig.4D, respectively. It is clear from these figures that GCE coated by GO film has superior electrical conductivity than others, which can be attributed to the introduction of GO with huge π electron conjugation system. A slight increase in the impedance of charge transfer can be observed after the basal electrode is modified by GO-AZO-1, which corresponds to inferior electrical conductivity of small organic molecules [40]. The charge transport resistance of BOD-based electrode is only slightly higher than that of GCE modified by GO-AZO-1.

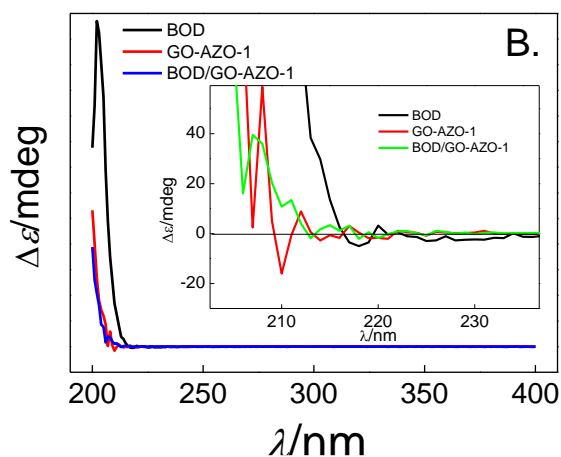


Figure 4. B CD spectra of PBS with dissolved BOD, thin film of GO-AZO-1, and BOD/GO-AZO-1 nanocomplex membrane

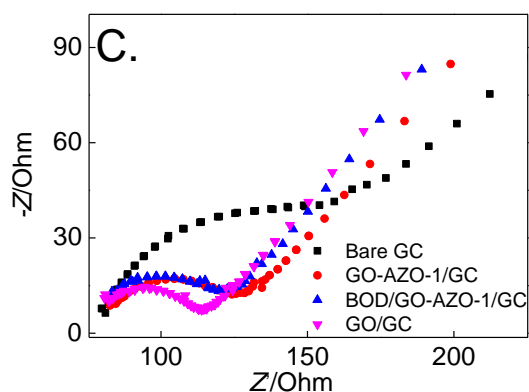


Figure 4. C EIS spectra of bare GCE, basal GCE modified by GO, GO-AZO-1/GCE, and BOD-based electrode, i.e., BOD/GO-AZO-1/GCE in oxygen-free electrolyte containing 5 mmol/L $K_3Fe(CN)_6$ + 0.1 mol/L KCl

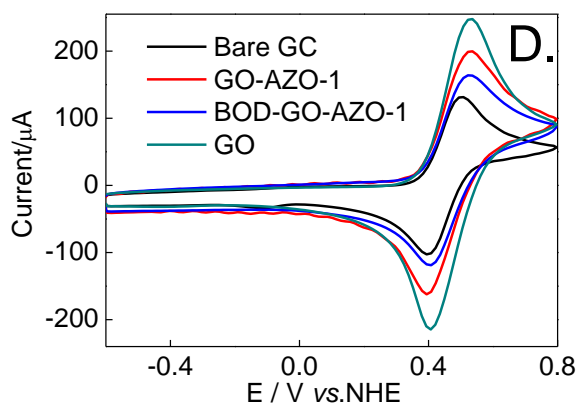


Figure 4. D CV curves of four electrodes: bare GC, GO/GC, GO-AZO-1/GC, and BOD/GO-AZO-1/GC in the same electrolyte as described in Fig.4C, where the sweep rate is 100 mV/s

However, the CV curves of BOD/GO-AZO-1/GC and GO-AZO-1/GC are inconsistent. This implies that the redox current decreases in GO-AZO-1 with BOD integration. Therefore, it can be inferred that interaction between enzyme molecules and probing species can hamper the dynamics of redox process for dissolved electro-active species. This inference is supported by the result of FRS measurements, which revealed that the characteristic fluorescence band corresponding to surface amino acids in BOD is sharply attenuated with the increase in the concentration of $K_3Fe(CN)_6$ in electrolyte (data not shown).

3.2 Direct electrochemical behavior, catalytic activity toward ORR, and light-driven energy conversion of BOD-based electrode

Direct electrochemistry and ORR catalytic activity of BOD-based electrode were characterized by CV, and the results are shown in Fig.5A. A pair of asymmetrical redox bands (ratio of oxidation peak current vs. reduction one ($i_{p,a}/i_{p,c}$) = 1.8 and potential gap = 345 mV) can be observed in the i-E curve of GO-AZO-1/GC in oxygen-free aqueous solution. Similar redox peak with higher integrated area can be identified in the CV curve of BOD/GO-AZO-1/GC in the same electrolyte. The former electrochemical signal should be attributed to the redox process of electroactive species within GO-AZO-1. Quasi-reversibility of redox peak implies that the reducing groups can be easily oxidized, but the reverse reaction is relatively difficult. Similar redox band is detected in CV curve of electrode coated with GO in nitrogen-bubbled solution, and no apparent electrochemical signal is discerned in the CV curve of basal GCE capped by thin film of AZO-1 (data not shown). This implies that the redox groups on the surface of GO can act as the primary site of electron transport. Further, it may be noted that the amount of electroactive species deduced from the mean integration area under the redox peaks of BOD-based electrode (4.34×10^{-9} mol) is higher slightly than that of reference electrode GO-AZO-1/GC (3.37×10^{-9} mol). Reasonably, the increased amount of electroactive species can be considered as the portion of electrically wired BOD molecules on the surface of GO-AZO-1 nanocomposite. Accordingly, it can be inferred that the partial enzyme molecules immobilized onto GO-AZO-1 nano-complex could mediate electron transport between redox species within GO-AZO-1 and conductive surface of supporter. Furthermore, the ORR catalytic activity and relevant dynamical parameters of BOD-based electrode can be obtained according to an earlier described method [41]. It is evident in Fig.5A that both electrodes (GO-AZO-1/GC and BOD-based electrode) exhibit high ORR catalytic activity, and the latter promotes the catalytic efficiency significantly. This assertion is based on the observation of an apparent positive shift in the onset potential of ORR for BOD-based electrode (320 mV) with respect to that of GO-AZO-1/GC (130 mV). The former value is close to the potential of T_1 site in BOD molecule (~ 490 mV) [42]. This implies that the combination of BOD with AZO-1 can increase the active energy of charge transfer between the primary electron acceptor on GO and T_1 site within BOD. It should be noted that no catalytic current is detected for basal electrode modified by thin film of AZO-1 with BOD tethering (data not presented). However, efficient binding and consequent transformation of oxygen molecules on the interface of AZO-1 with BOD linkage can be achieved. This conclusion is based on the determined consistency of dissolved oxygen. This suggests

that the amount of oxygen molecules in electrolyte is reduced to approximately 24.8% of the initial amount after the electrode coated by a thin film of AZO-1 with BOD integration is incubated in air-saturated solution for 6 h. Furthermore, turnover frequency of ORR for BOD-based electrode is estimated as $4.4 \times 10^{-2} \text{ s}^{-1}$ according to an earlier described equation [41].

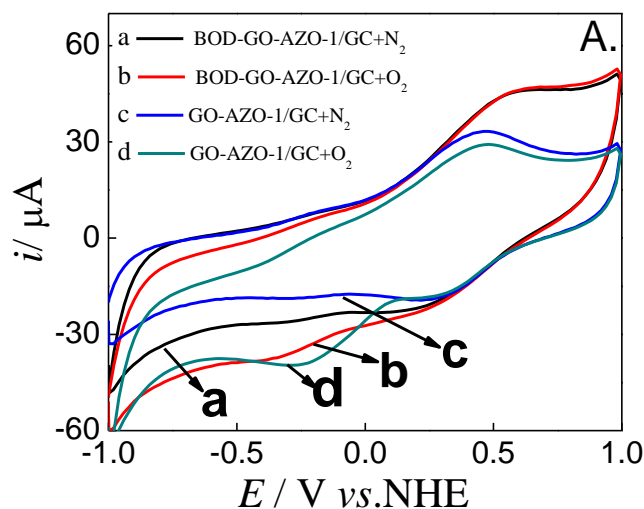


Figure 5. A Direct electrochemistry and ORR catalytic activity of BOD/GO-AZO-1/GC in PBS (pH = 4.4) characterized by CV with potential sweep rate of 50 mV/s

A series of i - E curves for BOD/GO-AZO-1/GC in PBS without dissolved oxygen molecules and external electron mediator obtained at variable scan rates are shown in Fig.5B. It is obvious that the currents of redox peaks are enhanced with the increase in sweep rate, and the ratio $i_{p,a}/i_{p,c}$ remains stable at variable scan rates of potential. The oxidation peak current of main redox band was obtained from the deconvolution of sequential oxidation waves in DPV curves as described earlier [43]. The potential gap between redox peaks does not show significant shift with the increase in the potential scan rates. The redox process occurring on the surface of BOD-based electrode can be ascribed to a diffusionless, typical surface confined mode of direct electron transfer (DET) [44-45]. It should be noted that a blunt side peak at high scan rate and a second reduction peak at negative potential (~ -690 mV) are observed in Fig.5B. It indicates the existence of additional redox species besides electroactive groups on GO. This electrochemical signal can be attributed to the composite of T_1 Cu within BOD in coordination with AZO-1 of nano-complex. This is consistent with the experimental results of FRS and UV-vis spectroscopy.

The results of DPV measurements also validate the above conclusions. The DPV curves of static BOD/GO-AZO-1/GC in oxygen-free PBS obtained at variable pulse heights are shown in Fig.5C (a: positive sweeping, b: negative sweeping). Two oxidation bands at small pulse height and one oxidation peak at large pulse height can be observed during positive scanning. The peak potentials of these bands show a negative shift with the increase in pulse height.

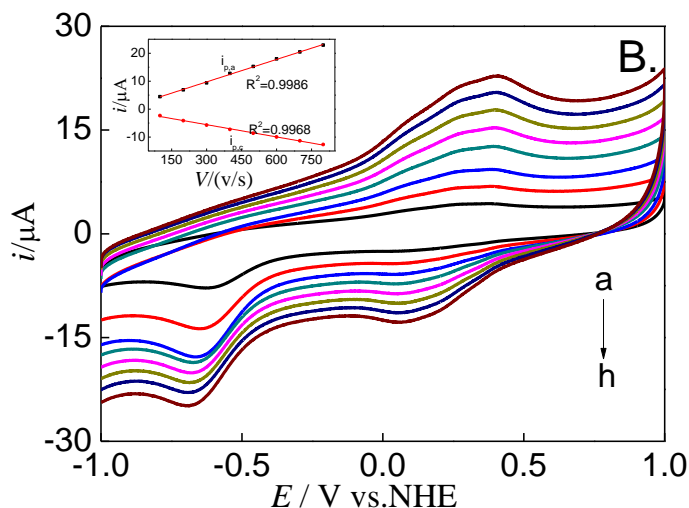


Figure 5. B CV curves of static BOD/GO-AZO-1/GC in oxygen-free PBS (pH = 4.4) without external electron relay recorded at variable scan rates of potential (curves a-h: 100, 200, 300, 400, 500, 600, 700, and 800 mV/s, respectively). Inset: linear-fitting plots of redox peak current vs. potential sweep rate

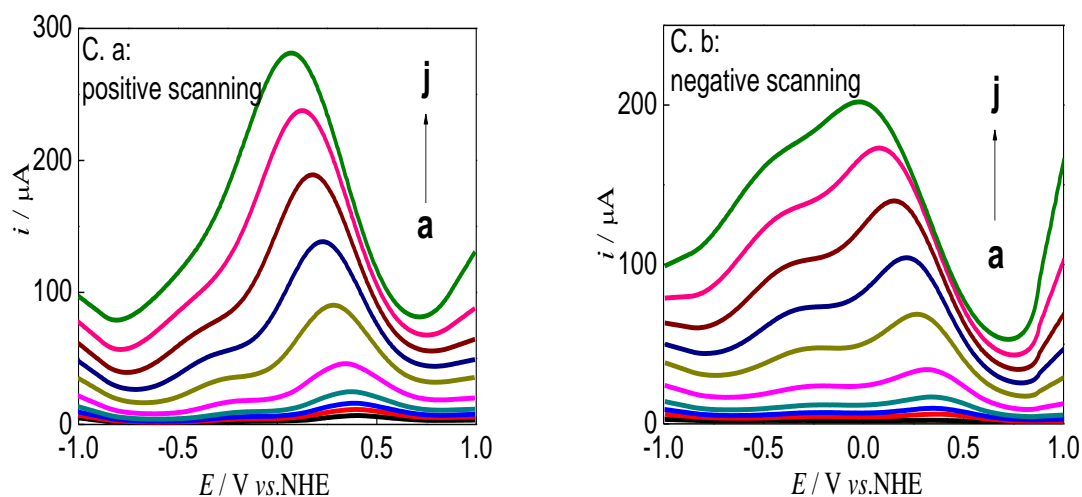


Figure 5. C DPV curves of static BOD-based electrode in deaerated PBS (pH = 4.4) recorded at 100 mV/s and different pulse heights (curves a-j in both figures represent the following pulse heights: 10, 20, 30, 50, 100, 200, 300, 400, 500, and 600 mV, respectively); positive scanning from -1.0 to 1.0 V, negative scanning from 1.0 to -1.0 V

Two reduction peaks could be observed in the process of negative sweeping at both large and small pulse heights. A negative shift in peak potential with the increase in pulse height is also observed during negative potential scanning. It can be inferred from these results that redox species within GO-AZO-1 nanocomplex exhibits superior electrochemical activity than partial T₁ site in complexation with AZO-1. Consecutive redox reactions occur between electro-active groups on GO and composite

of BOD in combination with AZO-1 at low pulse height, and redox process of such composite is suppressed at large pulse height. This implies that the existence of abutting ligation between T₁ site of BOD and AZO-1 anchored on GO can degrade the efficiencies of electron transfer and ORR catalysis in the long run. The result is different from that of similar system reported earlier [26] indicating the appearance of single redox band .

The apparent rate of heterogeneous electron transfer can be easily estimated to be 0.19 s⁻¹ from the curve of potential difference between redox bands for BOD-based electrode vs. logarithm of potential scan rate (see Fig.5D), which is in agreement with earlier studies [40,42]. This value is lower than that of other similar electrodes with multi-copper redox protein molecules immobilization (e.g., DET rate constant (1.3 s⁻¹) for an MCO based electrode with dendrimer-nano-gold particle composite as supporter [40]). The unfavorable dynamics of direct electrochemistry can be attributed to the poor electrochemical activity of redox groups on GO and composite of partial T₁ site in BOD combined with AZO-1.

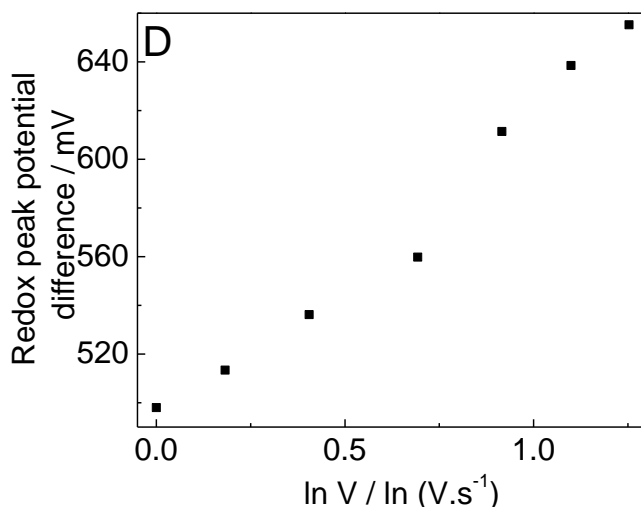


Figure 5. D Dependence of potential difference between oxidation and reduction peaks on the logarithm of potential scan rate for BOD/GO-AZO-1/GC in electrolyte in the absence of substrate and external electron relay

The CA curve of BOD-based electrode in PBS under magnetic stirring with variable consistency levels of substrate is shown in Fig.6A. Inset of Fig.6A shows the Lineweaver-Burk plot for the catalysis of ORR by BOD-based electrode. The steady current response of BOD-induced ORR linearly increases with the increase in oxygen content of PBS within the testing range of substrate concentration. The detection limit of BOD-based electrochemical sensor to O₂ is obtained as 0.1 μmol/L according to an earlier described method [46], which is half of that for similar enzyme-based electrode [26]. The sensitivity of BOD-based electrode to oxygen molecules is estimated to be 2.35 μA L/μmol, which is much higher than that of electrode based on the incorporation of multi-copper oxidase into polyaniline-C₆O₂O₄ nanocomposite (0.006 μA L/μmol) [26] and is only 1/12 of that of

electrode based on the immobilization of multi-copper oxidase on Chitosan-multiwall carbon nanotubes ($27.3 \mu\text{A L}/\mu\text{mol}$) [32]. The Michaelis constant (K_M) is obtained as $30.2 \mu\text{mol/L}$ from the reciprocal plot in inset of Fig.6A, and this value is much lower than that reported earlier (3.2 mmol/L) [32]. This indicates that GO-AZO-1 with BOD immobilization exhibits a high affinity to dissolved O_2 , which can be attributed to its outstanding capability to entrap oxygen molecules and minor interference in the oxygen binding process from mutual interactions described early. Almost an identical variation in the oxygen content of PBS determined by Clark oxygen electrode can be observed for GO with BOD attachment and GO-AZO-1 nanocomplex with BOD incorporation before and after the incubation in air-saturated electrolyte. The apparent oxygen binding rate constant of BOD entrapment into GO-AZO-1 is estimated to be $\sim 0.1 \text{ s}^{-1}$ from Fig.6A according to a method reported earlier [47].

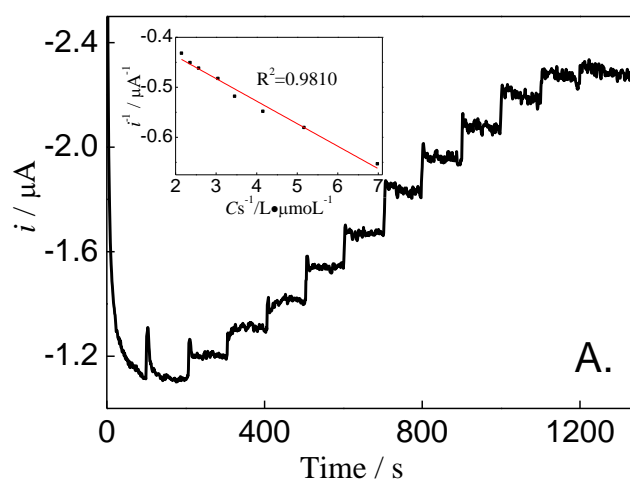


Figure 6. A CA curves of static BOD/GO-AZO-1/GC PBS (pH=4.4) under magnetic stirring with variable concentration of dissolved O_2 , where the applied potential is -450 mV . Inset: double reciprocal plot of steady current response vs. concentration of substrate

The CV curves of BOD/GO-AZO-1/GC in oxygen-free electrolyte with varying pH and the corresponding linear-fit plots between mean value of redox peak potential and pH of PBS are shown in Fig.6B and its inset, respectively. A negative shift in oxidation and reduction potential of BOD-based electrode with the increase in pH value of aqueous solution is observed in Fig.6B. The relationship between mean value of redox peak potential of BOD/GO-AZO-1/GC and pH value of electrolyte is consistent with the Nernst equation. The number of H^+ ions and electrons involved in the electrochemical reaction occurring on the surface of BOD-based electrode is roughly estimated as 3.0 and 4.0 according to the slope of peak potential vs. pH plot (inset, Fig.6B). This result is in agreement with the previously described nature of heterogeneous electron transfer for BOD-based electrode and the equilibrium of azo-quinoid tautomerism at distinct pH value reported earlier [28, 36].

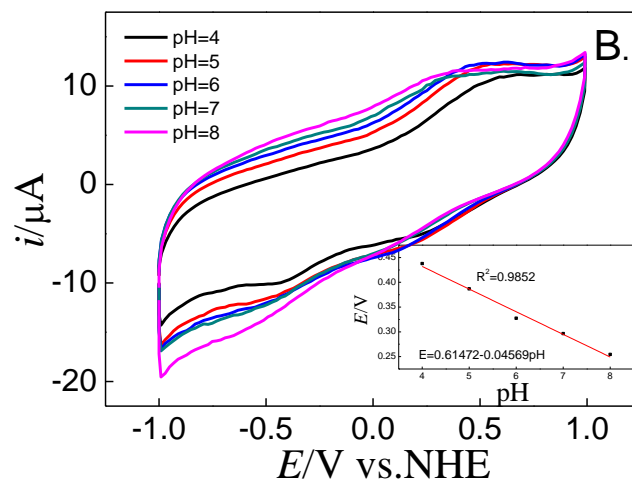


Figure 6. B CV curves of BOD-based electrode in nitrogen-bubbled PBS with variable pH value obtained at a scan rate of 100 mV/s; inset: calibration plot of mean value of redox peak potential vs. pH of electrolyte

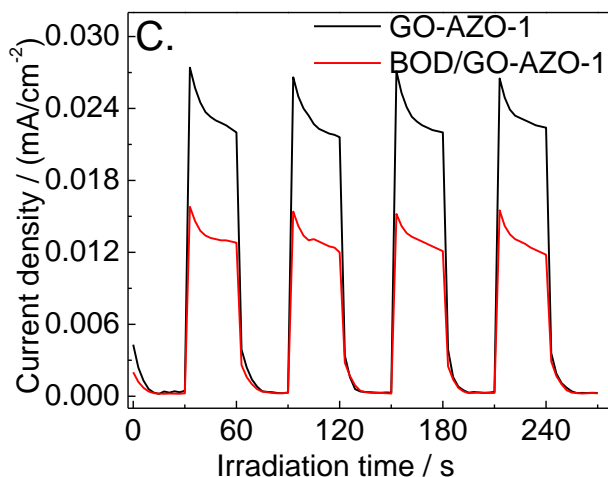


Figure 6. C Dependence of photocurrent density on the irradiation span for GO-AZO-1 nanocomplex and nanocomposite with BOD anchoring

The photoelectro-chemical response of BOD-based electrode in oxygen-saturated electrolyte as a function of illumination time of samples is shown in Fig.6C. The photocurrent response is minor when the light source is turned off, and the photocurrent density is drastically enhanced when it is turned on. The photoelectro-chemical activity decreases sharply when the illumination source is again turned off. This behavior is observed in both the systems referred here. The steady photocurrent response for both the cases is essentially retained and reproducible under a couple of on-off cycles of incident light. The steady photocurrent density of GO-AZO-1 is ~ 0.023 mA/cm², which is close to the maximum photoelectrochemical current density of reduced GO decorated TiO₂ compound (0.018 mA/cm²) [48]. The favorable photocurrent density of GO-AZO-1 implies that the electron-hole separation and electron transfer from valence band to conductive band are possible with low active

energy. However, the photoelectrochemical activity of nanocomplex with BOD integration is significantly degraded, as shown in Fig.6C, which can be attributed to the fact that the binding of T₁ Cu within BOD with AZO-1 anchored on GO forms a compound with low stability and inferior capability to transport electrons.

All these results are validated by the incident photon to current conversion efficiency (IPCE) curves shown in Fig.6D. The IPCE of both the systems is determined using an earlier described method [48]. GO functionalized by AZO-1 exhibits higher IPCE values within the range of applied wavelength than GO-AZO-1 connected with BOD. This result verifies the desirable efficiency of incident light utilization. Additional difference between the locations of secondary peak in IPCE curves of the two systems may be related to the efficient electron transport and abutting coordination as discussed previously.

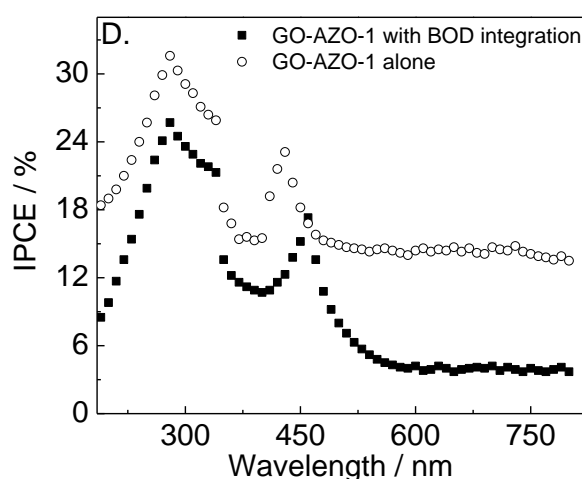
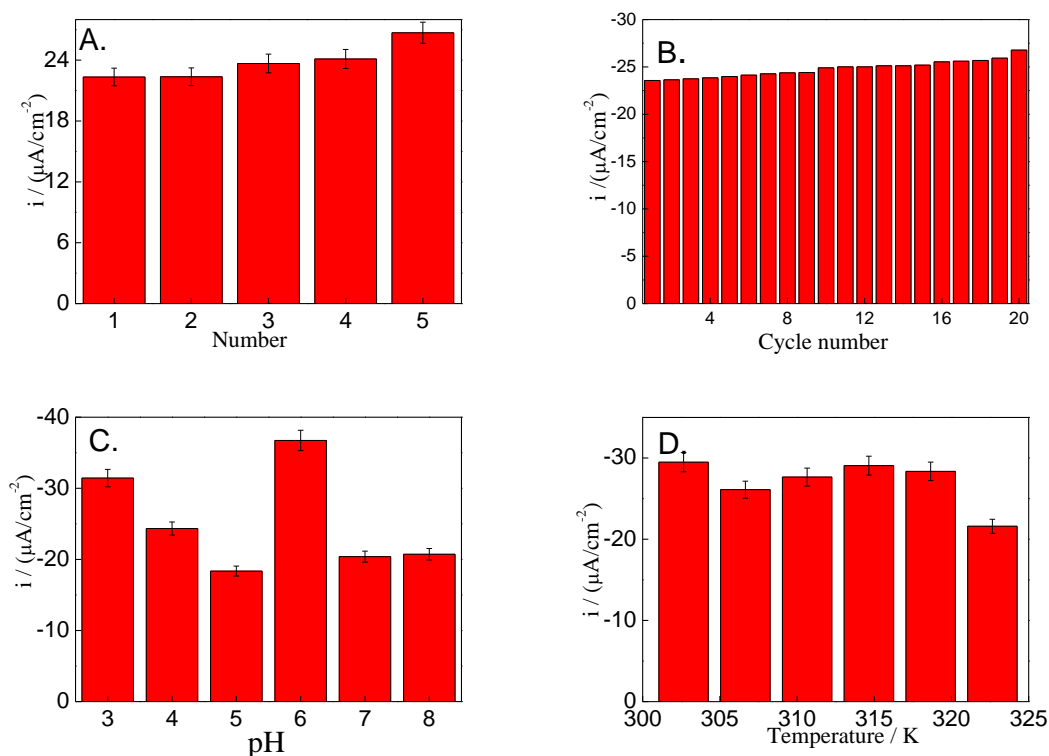


Figure 6. D Relationship between incident photon to current conversion efficiency (IPCE) and wavelength for GO-AZO-1 and BOD/GO-AZO-1

The repeatability, recycling performance, pH dependence, and impact of operation temperature on catalytic efficiency of BOD-based electrode under solar irradiation are shown in Fig.7(A-D), respectively. The ORR catalytic performance of as-prepared BOD-based electrode is evaluated by CV, as demonstrated in Fig.5A. Fig.7A reveals relatively minor difference in catalytic current densities among the five electrodes prepared using the same procedure. No noticeable decay in catalytic current density of ORR for BOD-based electrode is observed in Fig.7B even after 20 usage cycles. All these results indicate that the BOD-based electrode exhibits excellent reproducibility and recyclability. It is clear from Fig.7C that the BOD-based electrode displays high ORR catalytic efficiency at pH=6, and the second optimal pH value is 3.0. The former is consistent with the nature of free blue multi-copper oxidase [49], and it proves that the favorable ORR catalytic efficiency of GO-AZO-1 with BOD immobilization can be retained to a great extent even in the presence of adjacent complexation as described earlier. The latter is not consistent with the dependence of catalytic activity on pH for both the systems: free enzyme and immobilized enzyme [49]. This should be related to the unique chemical environment of enzyme matrix that induces inherent catalytic function of immobilized BOD.

Moreover, BOD-based electrode exhibits good thermal stability in ORR catalytic function within the temperature range of 300-320 K, as shown in Fig.7D. This can be attributed to the combination of enzyme with GO-AZO-1 leading to agglomeration of BOD on the surface of enzyme carrier as described earlier. This aggregation state of attached BOD is conducive for retaining the configuration of oxygen binding sites in BOD. The catalytic performance of GO-AZO-1 with BOD immobilization decreases considerably when the operation temperature is higher than 323 K, which can be ascribed to the partial detachment of BOD from enzyme matrix and distortion in configuration of cofactors in BOD. All these factors can lead to the loss of oxygen binding capability of entrapped enzyme molecules. This conclusion is based on the fact that the absorbance band at 279.6 nm of nanocomposite with BOD incorporation significantly weakens when the operation temperature is up to 325 K. Furthermore, the concentration of oxygen molecules in PBS at 325 K after the incubation of nanocomplex with immobilized BOD in electrolyte for 8 h is almost identical to the initial value of O_2 consistency in air-saturated electrolyte. It should be noted that the negative impact of mutual interactions between AZO-1 and redox sites within immobilized BOD on the ORR catalytic function of BOD-based electrode cannot be ignored. This inference is supported by the long-term usability of catalytic effect on ORR shown in Fig.7E. The catalytic current is reduced by approximately 27% loss after the storage of BOD-based electrode for 7 days, and ~44% of initial value of catalytic ORR is retained after 14 days of incubation. Eventually, after 21 days of incubation, less than 8% of maximal current for BOD-induced ORR is retained. This result is consistent with the trend of decay in efficiency of heterogeneous electron transport for BOD/GO-AZO-1/GC (determined parameters for the storage of BOD-based electrode for 7, 14, and 21 days are 0.15, 0.097, and 0.019, respectively).



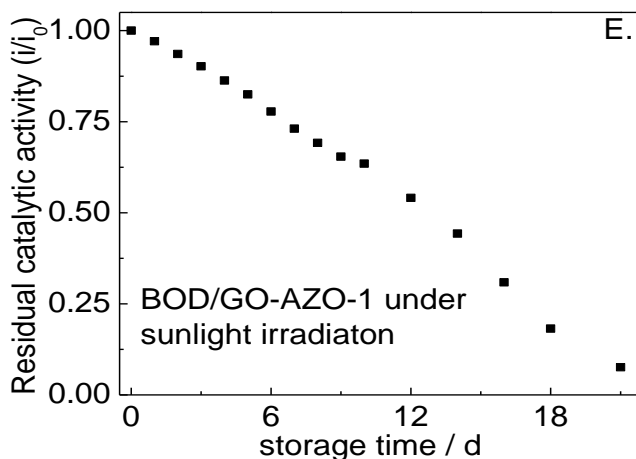


Figure 7. Reproducibility (A), cyclic usability (B), acid-base endurance (C), thermal stability (D), and long-term usability (E) in enzyme-induced ORR catalysis of BOD-based electrode under solar illumination, which are characterized by CV, as illustrated in Fig.5A

4. CONCLUSION

Surface-tailored GO by AZO-1 enzyme carrier was used to incorporate BOD via complicated mutual interactions between GO-AZO-1 and cofactors in BOD including covalent bonding and abutting coordination. BOD-based electrode was prepared using the nanocomposite with BOD incorporation through wet-coating method. The aggregation state of protein on matrix, surface features, structural characteristics, and physiochemical properties of GO-AZO-1 nanocomplex with BOD tethering (i.e., BOD/GO-AZO-1) were characterized by a variety of techniques including spectrometry, GFAAS, SEM, TEM, TGA, and electrochemical techniques. The photoelectrocatalytic performance of BOD/GO-AZO-1 toward ORR was evaluated by chronoamperometry. The measurement results revealed that BOD/GO-AZO-1 exhibited excellent properties such as desirable robustness, good thermal stability, and high catalytic efficiency. The partial side-directed binding between T₁ Cu site in BOD and AZO-1 formed a composite with greatly suppressed fluorescence emission and caused partial ordered arrangement of protein on the surface of nanocomposite, leading to the formation of a unique micelle-like structure. The redox groups within GO-AZO-1 exhibited excellent electrochemical activity and acted as the primary electron acceptor. The cofactors in BOD only played a role in the electron relay process. The electrochemical reaction of the as-prepared BOD-based electrode was categorized as a typical quasi-reversible surface-controlled reaction involving three H⁺ ions and four electrons. The complex interactions between nanocomplex and incorporated protein molecules enhanced the active energy of ORR. Such interactions did not hinder the substrate binding on cofactors of entrapped BOD molecules severely. The intermittent switching between “on” and “off” states under incident irradiation could be achieved. for BOD/GO-AZO-1. The IPCE value of BOD/GO-AZO-1 was lower than that of GO-AZO-1 due to the negative impact of adjacent complexation on illumination utilization.

ACKNOWLEDGEMENTS

The research presented in this submission was subsidized by the National Natural Science Foundation of China (No. 31560249) and the “13th five-year” plan for key discipline chemistry, Xinjiang normal university.

References

1. K. Abinaya, S. Karthikaikumar, K. Sudha, S. Sundharamurthi, A. Elangovan and P. Kalimuthu, *Appl. Catal., B.*, 242 (2019) 293.
2. B. Cakiroglu and M. Ozacar, *Biosens. Bioelectron.*, 119 (2018) 34.
3. L. Han, S.J. Guo, P. Wang and S.J. Dong, *Adv. Energy Mater.*, 5 (2015) 1400424.
4. A. Koushanpour, N. Guz, M. Gamella and E. Katz, *J. Electrochem. Soc.*, 5 (2016) M3037.
5. S. Liu, J. Q. Tian, L. Wang, Y. L. Luo, W. B. Lu and X. P. Sun, *Biosens. Bioelectron.*, 26 (2011) 4491.
6. T. F. Yeh, J. M. Syu, C. Cheng, T. H. Chang and H. Teng, *Adv. Funct. Mater.*, 20 (2010) 2255.
7. W. S. Zhao, X. Y. Li, Z. Wen, X. L. Niu, Q. F. Shen, Z. L. Sun, R. X. Dong and W. Sun, *Int. J. Electrochem. Sci.*, 12 (2017) 4025.
8. H. P. Huang, L. Xu, Y. F. Yue and L. P. Jiang, *Chinese J. Inorg. Chem.*, 32 (2016) 2034.
9. Y. L. Niu, X. Q. Huang and W. H. Hu, *J. Power Sources*, 332 (2016) 305.
10. L. X. Gao, J. L. Xie, X. Q. Ma, M. Li and L. Yu, *Nanoscale Res. Lett.*, 12 (2017) 1.
11. L. Wu, W. M. Yin, K. Tang, D. Li, K. Shao, Y. P. Zuo, J. Ma, J. W. Liu and H. Y. Han, *Anal. Chim. Acta*, 933 (2016) 89.
12. Z. P. Kang, K. L. Jiao, J. Cheng, R. Y. Peng, S. Q. Jiao and Z. Q. Hu, *Biosens. Bioelectron.*, 101 (2018) 60.
13. X. L. Li, Q. Tang, C. C. Guo, R. Ma, W. B. Chang and C. B. Gong, *Chem. J. Chinese U.*, 32 (2011) 2706.
14. K. So, Y. Kitazumi, O. Shirai and K. Kano, *J. Electroanal. Chem.*, 783 (2016) 316.
15. X. C. Huang, L. L. Zhang, Z. Zhang, S. Guo, H. Shang, Y. B. Li and J. Liu, *Biosens. Bioelectron.*, 124 (2019) 40.
16. A. Korani and A. Salimi, *Electrochim. Acta*, 185 (2015) 90.
17. M. T. Meredith, M. Minson, D. Hickey, K. Artyushkova, D. T. Glatzhofer and S. D. Minteer, *ACS Catal.*, 1 (2011) 1683.
18. S. Trohalaki, R. Pachter, H. R. Luckarift and G. R. Johnson, *Fuel Cells Bull.*, 12 (2012) 656.
19. H. Zhang, J. Q. Luo, S. S. Li, J. M. Woodley and Y. H. Wan, *Chem. Eng. J.*, 359 (2019) 982.
20. H. M. Albishri and D. A. El-Hady, *Talanta*, 200 (2019) 107.
21. F. Wang, S. X. Zhao, H. Zeng and W. S. Huo, *Int. J. Electrochem. Sci.*, 15 (2020) 6645.
22. W. Zheng, H. M. Zhou, Y. F. Zheng and N. Wang, *Chem. Phys. Lett.*, 457 (2008) 381.
23. R. Wang, Y. Yin, R. Wang, Y. Xie, B. Ge, Z. Li, Z. Li, J. Shi and J. Chang, *J. Lumin.*, 144 (2013) 79.
24. X. H. Zhou, X. R. Huang, L. H. Liu, X. Bai and H. C. Shi, *Rsc Adv.*, 3 (2013) 18036.
25. Q. H. Wang, Preparation of Throwable Electrode based on ITO and its Application in biomolecule detection, Nantong University, China, 2016, 2.
26. Y. Yang, W. S. Huo, Z. Zhou, Q. Zhang and H. Zeng, *Chinese J. Inorg. Chem.*, 32 (2016) 2117.
27. P. Ramírez, N. Mano, R. Andreu, T. Ruzgas, A. Heller, L. Gorton and S. Shleev, *Biochim. Biophys. Acta*, 1777 (2008) 1364.
28. W. Feng, C. Q. Qin and Y. Y. Feng, Zobenzen/graphene hybrid materials for high-energy and long-term solar energy storage, National Conference on Polymer Materials Science and Engineering Abstract, NingBo, China, 2016, 900.
29. J. Huang, J. Y. Zhou, H. Y. Xiao, S. Y. Long and J. T. Wang, *Acta Chim. Sinica*, 63 (2005) 1343.

30. W. Sun, Z. L. Sun, L. Q. Zhang, X.W. Qi, G. J. Li, J. Wu and M. Wang, *Colloids Surf. B*, 101 (2013) 177.
31. H. Y. Zhao, H. M. Zhou, J. X. Zhang, W. Zhang and Y. F. Zheng, *Biosens. Bioelectron.*, 25 (2009) 463.
32. Y. Liu, X. H. Qu, H. W. Guo, H. J. Chen, B. F. Liu and S. J. Dong, *Biosens. Bioelectron.*, 21 (2006) 2195.
33. Y. L. Wang, Z. C. Wang, Y. P. Rui and M. G. Li, *Biosens. Bioelectron.*, 64 (2015) 57.
34. S. G. Hong, J. H. Kim, R. E. Kim, S. J. Kwon, D. W. Kim, H. T. Jung, J. S. Dordick and J. Kim, *Biotechnol. Bioprocess Eng.*, 21 (2016) 573.
35. H. P. Liu, Preparation of Photoreactive azobenzene chromophore/Graphene complexes, Tianjin University, China, 2012, 22.
36. P. Fan, Z. Jin, Y. Pan and G. J. Liu, *Chem. J. Chinese U.*, 30 (2009) 724.
37. H. Mao, B. F. Cai, B. Zhao and Z. W. Wang, *Chinese J. Appl. Chem.*, 26 (2009) 1332.
38. K. Piontek, M. Antorini and T. Choinowski, *J. Biol. Chem.*, 277 (2002) 37663.
39. A. E. Palmer, D. W. Randall, F. Xu and E. I. Solomon, *J. Am. Chem. Soc.*, 121 (1999) 7138.
40. M. A. Rahman, H. B. Noh and Y. B. Shim, *Anal. Chem.*, 80 (2008) 8020.
41. S. Tsujimura, Y. Kamitaka and K. Kano, *Fuel Cells Bull.*, 7 (2007) 463.
42. S. Shleev, J. Tkac, A. Christenson, T. Ruzgas, A. I. Yaropolov, J. W. Whittaker and L. Gorton, *Biosens. Bioelectron.*, 20 (2005) 2517.
43. E. Katz, V. Heleg-Shabtai, I. Willner, H. K. Rauand W. Haehnel, *Angew. Chem. Int. Ed.*, 37 (1998) 3253.
44. H. J. Qiu, C. X. Xu, X. R. Huang, Y. Ding, Y. B. Qu and P. J. Gao, *J. Phys. Chem. C*, 112 (2008) 14781.
45. J. D. Qiu, H. P. Peng, R. P. Liang and X. H. Xia, *Biosens. Bioelectron.*, 25 (2010) 1447.
46. Y. Zhang, G. M. Zeng, L. Tang, D. L. Huang, X. Y. Jiang and Y. N. Chen, *Biosens. Bioelectron.*, 22 (2007) 2121.
47. W. E. Farneth, B. A. Diner, T. D. Gierke and M. B. D'Amore, *J. Electroanal. Chem.*, 581 (2005) 190.
48. S. C. Wang, J. S. Cai, J. J. Mao, S. H. Li, J. L. Shen, S. W. Gao, J. Y. Huang, X. Q. Wang, I. P. Parkin and Y. K. Lai, *Appl. Surf. Sci.*, 467 (2019) 45.
49. D. S. Jiang, S. Y. Long, J. Huang, H. Y. Xiao and J. Y. Zhou, *Biochem. Eng. J.*, 25 (2005) 15.